ADVANCED FUNCTIONAL MATERIALS
www.afm-journal.de

Monochromatic Wide-Angle Optical Edge Detection Enabled by a Three-Dimensional Soft Photonic Crystal

*Zhiyao Xie, Quanming Chen, Cheng Ouyang, Qiguang Wang, and Wei Hu**

Optical edge detection is attractive in real-time image information compression, image recognition, and three-dimensional reconstructions due to its fast response and low power consumption. Liquid crystal planar optics is widely used to carry out optical differentiation due to its dynamic functionality. However, it still suffers from edge distortions and contrast reductions for oblique incidence, severely restricting its application in monochromatic wide-angle optical edge detections. Here, a blue phase liquid crystal *q*-plate based 4*f* imaging system is developed to solve the above problems. With the photopatterned three-dimensional photonic crystal, the same spiral phase is encoded omnidirectionally to all reflected light, thus avoiding oblique incidence-induced edge distortions and image contrast reduction. Moreover, the electrostriction-induced lattice extension is further adopted to compensate for the angle-dependent wavelength shift, thus realizing a monochromatic wide-angle optical edge detection. The inherent circular polarization-dependent phase modulation enables simultaneous optical edge imaging and bright-field imaging, which makes the image detection more accurate. This work explores the potential of three-dimensional soft photonic crystals in optics and photonics, supplies a practical platform for active monochromatic wide-angle optical edge detection, and will be widely applied in LiDAR, machine vision, and biomedical imaging.

1. Introduction

Compared with traditional digital electronic image processing, optical edge detection has attracted more and more attention in autonomous vehicles,[1] microscopic biomonitoring,[2] and three-dimensional (3D) reconstructions[3] due to the merits of fast response and low power consumption compared to traditional digital electronic image processing.[4] It is usually carried out via optical differential operation with distinct physical effects, such as photonic spin Hall effect,[5] Goos-Hänchen effect,[6] spin–orbit coupling effect,[7] interference effect associated with surface plasmon excitation[8] and spiral phase contrast.[9] The above optical differentiation can be accomplished by inserting specifically designed photonic crystals,[10] metasurfaces[11] and uniaxial crystals[7] in front of a camera. Optical edge detection is suitable for real-time big-data processing in real applications for 3D surrounding reconstructions as well as for object recognition. Recently, compact optical edge imaging systems with adaptive multiple functions have been specially pursued. Correspondingly, researchers have developed various dynamic planar optics to meet these new requirements.

Liquid crystals (LCs) are excellent stimuli-responsive materials with optical anisotropy ready to be reversibly tuned by various external stimuli. With LCs, planar optics of dynamic functionalities can be realized via geometric phase encoding,[12] superstructure self-organization,[13] or integration with a metasurface.[14] They have been widely adopted in optical edge detection over the past few years.[15] Alternations among 0th, 1st and 2nd order differentiations were demonstrated via electrically tuning the tilt angle of the LC inside a polarization grating and manually adjusting the incident polarization.[16] Ultra-fast switching between horizontal and vertical edge detections were presented on the basis of the electrically driven optical axes rotations of ferroelectric LCs.[17] With photopatterned cholesteric LCs (CLCs), whose one-dimensional (1D) helical structure exhibits spin-selective Bragg reflections, color-selective optical edge detection[18] and spin-selective simultaneous bright field imaging and 2nd order spatial differentiation are realized.[19] For active optical edge detection, the above elements face two challenges for oblique incidence: firstly, the contrast of optical edge imaging is significantly reduced due to the deviation from the halfwave condition; secondly, the distortion of the spatial phase induces remarkable aberrations. Blue phase LCss (BPLCs) self-assemble into double twisted cylinders (DTCs) and further stack into body centered cubic (BP I) or simple cubic (BP II) lattices.[20] Therefore, it is widely used in optoelectronics fields such as displays,[21] anti-counterfeiting[20a] and lasers.[20b] Thanks to its unique 3D chiral photonic crystal features, the same geometric phase can be encoded to omnidirectionally reflected light.[22] However, the

Z. Xie, Q. Chen, C. Ouyang, Q. Wang, W. Hu
National Laboratory of Solid State Microstructures
Jiangsu Physical Science Research Center
College of Engineering and Applied Sciences
Nanjing University
Nanjing 210023, China
E-mail: huwei@nju.edu.cn
Q. Chen
Department of Electrical & Electronic Engineering
Southern University of Science and Technology
Shenzhen 518055, China

The ORCID identification number(s) for the author(s) of this article can be found under https://doi.org/10.1002/adfm.202500920

DOI: 10.1002/adfm.202500920

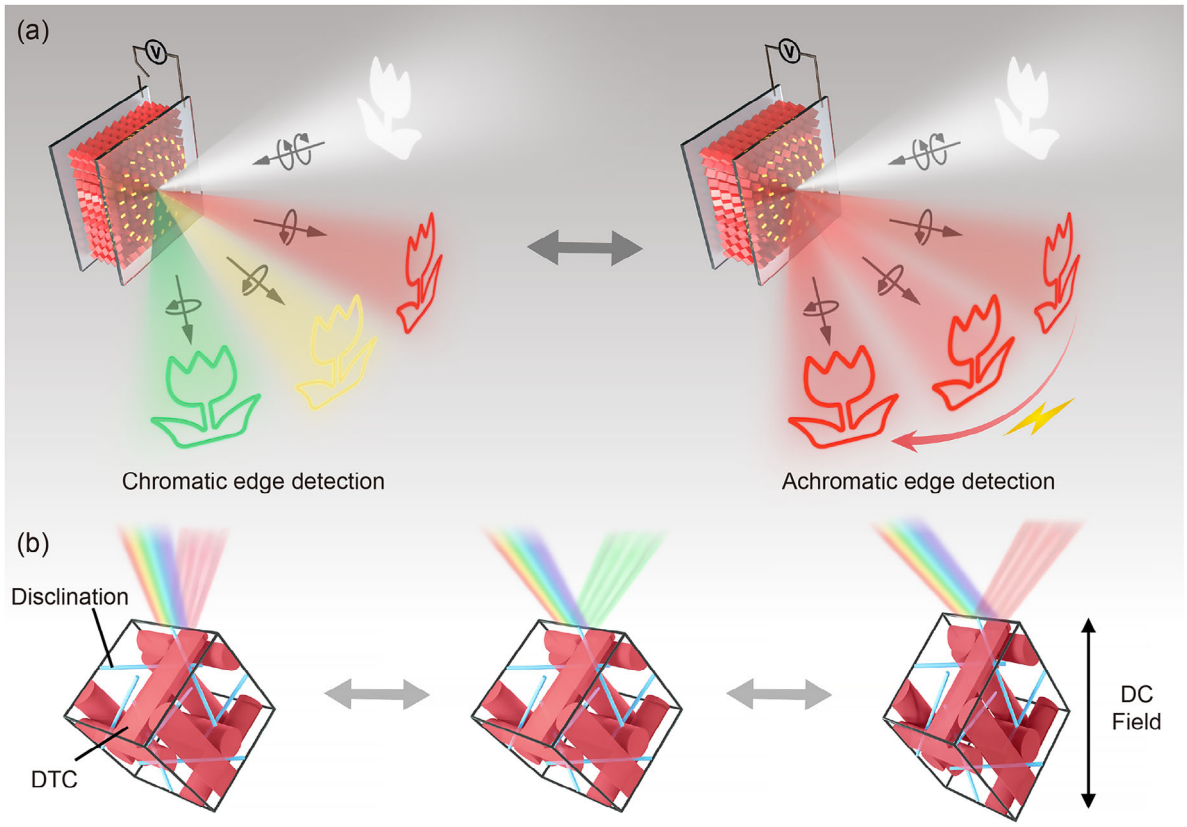

Figure 1. a) Schematic illustrations of optical edge imaging with angle-dependent reflective colors (left) and single wavelength optical edge imaging with a large FOV (right) based on a BPLC *q*-plate. b) Schematic illustrations of angle-dependent reflective colors and electrostriction induced wavelength-shift compensation. Red tubes represent DTCs and thin blue lines represent disclinations.

system exhibits a strong dependency of reflective colors on the incident angle.[23] If one can realize precise compensation for the angle-dependent wavelength shift via synchronously manipulating the lattice constant of the BPLC, the above challenges could be perfectly overcome. Fortunately, BPLC can easily change its crystal parameters or even phase states under external stimuli such as humidity,[24] light[25] and mechanical force,[26] enabling precise modulation of PBG. The electrically tunable BPLC[27] has been widely studied due to its reliable controllability and fast response. Under the electric field, BP exhibits various effects such as Kerr effect,[28] electrostriction,[27c] and electric field induced phase transition.[29] The electrostriction depicts the lattice constant variation of BPLC under the electric field, which usually leads to a shift in reflection wavelength.[27b,30]

Here, we prepare two BP I *q*-plates by photopatterning, which cover color ranges of green to blue and red to green as the incident angle increases, respectively. After direct current (DC) electrical fields are applied to these samples, their lattice constants are electrically extended, while the photopatterned superstructures remain undamaged. As a result, by properly varying the DC voltage, the incident angle dependent color shift can be accurately compensated by the lattice extension. By this means, single wavelength optical edge imaging is achieved within ±45° in high quality. It supplies a practical platform for wide view angle active optical edge detection and other optical applications including LiDAR, biomedical imaging, and space laser communication with high directional robustness requirements.

2. Results

2.1. Design and Principle

Figure 1a illustrates the BPLC *q*-plate ($q = 0.5$) for optical edge imaging. Since the [001] crystal direction keeps an angle of 28° with respect to the local alignment, the azimuthal orientation of the BPLC lattice can be precisely controlled by photopatterning.[23,31] Herein, the preset alignment $\beta(x, y)$ follows $\beta = 0.5\arctan(y/x)$.[32] When such a *q*-plate is placed in the Fourier plane of a 4*f* imaging system as an optical differentiator, light within the photonic bandgap (PBG) and of the same handedness as the helicity of the BPLC is selectively reflected and carries a geometric phase of $2\cdot\beta(x, y)$. Then the reflected light $E_{out}(x, y)$ and the incident light $E_{in}(x, y)$ follows:

$$E_{out}(x, y) = \frac{\partial E_{in}(x, y)}{\partial x} + i\frac{\partial E_{in}(x, y)}{\partial y} \quad (1)$$

Thereby, $E_{out}(x, y)$ and $E_{in}(x, y)$ exhibit a Two-dimensional first-order differential relationship (Derive details as shown in Note S1, Supporting Information). Simulations in Figure S1 (Supporting Information) show that the intensity of optical edges

is nonuniform and even distorted for cases of $q \neq \pm 0.5$. At the same time, light of orthogonal circular polarization or outside of the PBG transmits directly with a spatially uniform phase shift.[33] As a result, two distinct functions are established based on the BPLC q-plate: reflective optical edge imaging and transmissive bright-field imaging.

As a 3D photonic crystal, the geometric phase is encoded omnidirectionally to the photopatterned BPLC. As the Bragg–Berry phase is only encoded to the vector components in the x-y plane and is unrelated to the z component the Equation (1) is applicable even for large incident angles.[22] The narrowband optical edge detection limits the optical efficiency of the device, however, for active detection where lasers are usually used as light sources, this design is beneficial for suppressing the influence of background light and significantly increasing the Signal Noise Ratio. Notably, the central wavelength λ_c of the PBG satisfies Bragg's equation:[34]

$$\lambda_c = 2nd\cos\theta = \frac{2nd\cos\theta}{\sqrt{h^2 + k^2 + l^2}} \quad (2)$$

where h, k, and l represent the Miller indices of the lattice direction; the average refractive index $n = (2n_o + n_e)/3$, n_o and n_e are the ordinary and extraordinary refractive indices, respectively; d is the interplanar spacing of (h k l); a is the lattice constant; and θ is the angle between the light incidence and the crystal orientation [h k l]. Obviously, the BPLC q-plate exhibits angular dependence. As shown in the left image of Figure 1a, a blueshift of the PBG is observed for oblique incidence. To realize monochromatic wide-angle optical edge detection, the lattice constant should be precisely tuned to compensate for the angle-dependent color shift. The electrostriction of the BPLC can be introduced for compensation.[30] Under a DC electric field, the polymer network that captures cations stretches toward the negative electrode, and the BPLC lattice constant is enlarged as well due to the anchoring effect of the polymer.[35] As revealed in Figure 1b, the PBG blueshifts along with the increasing incident angle. While the lattice stretching induced by electrostriction can redshift the PBG back to its original λ_c (normal incidence). After compensation, single wavelength and large field of view (FOV) optical edge imaging can be accomplished (right image in Figure 1a).

2.2. Electrically Tuned PBG of BPLC

The detailed compositions and preparation process of BPLC samples M1 and M2 please refer to the experimental section, as well as Figures S2 and S3 (Supporting Information). The schematic illustration of the monodomain growth of the BPLC is shown in Figure S2 (Supporting Information), and design details of the BPLC q-plate are shown in Figure S3 (Supporting Information). The omnidirectional Bragg–Berry phase can be encoded to BP II as well. Here, BP I was chosen for its lower PBG is beneficial for optical edge detection and imaging. An alternating current (AC) electric field (1 kHz) is applied to the BPLC in the BP I phase for 1 min. The LC is driven to a homeotropic state and the system is heated to a temperature slightly lower than the BP II-BP I transition point by dielectric heating. After the electric field is removed, the uniform initial orientation successfully suppresses the multidomain generation and leads to a monodomain BP I follow the guidance of surface anchoring during the recrystallization process (comparison between polydomain and monodomain of BPLC as shown in Figure S4 (Supporting Information) and the principle of field induced single domain BP I as shown in Figure S2 (Supporting Information) The coexistence of DTC and disclination makes it difficult to stabilize the BP lattice. Therefore, BP typically only exists within a very narrow temperature range. By utilizing the strategy of polymer stabilization, researchers can stabilize the BP lattice and effectively extend the BP temperature range beyond 60 K.[36] Here, based on this strategy, the temperature range of the BPLC is expanded to cover room temperature. Additionally, the PBG of BPLC becomes temperature-independent after polymer stabilization (Figure S5, Supporting Information). Then a DC electric field E is applied perpendicularly to the cell in the range of 0 – 11.36 V μm^{-1}. As exhibited in **Figure 2a**, λ_c redshifted from 500 to 620 nm along with the increase of E. The color shift is reversible when the DC electric field is recycled. The drop of reflectance at higher fields is attributed to two facts: first, the number of reflection surfaces reduces during the lattice stretching in a fixed cell gap;[37] second, the reflectance of each reflection surface decreases due to the tilting of LC induced birefringence reduction. According to the reflection law, the reflectance of each interface is determined by the refractive index difference (i.e., birefringence). Due to the limited pitches in such a thin cell (7.7 μm), the total reflectance reduces significantly along with the tilting and unwinding of LC under the DC electric field. The tail of the reflection band on the short wave side under a DC electric field is attributed to the uneven distribution of the polymer network caused by the gradient of polymer light intensity.[34] Figure 2b shows the response of the PBG shift under DC electric fields of 0 and 11.36 V μm^{-1}. Here, we define the response time as the time interval between 10% and 90% PBG shift, and response times of 8.5 and 5.5 s are recorded, respectively. They correspond to the largest angle compensation. The response time for smaller angles is shorter compared to the above values. And the response time is expected to be drastically reduced via filling ferroelectric or ferroelectric nematic LCs into BPLC polymer templates. Even after 30 cycles of tuning, λ_c still exhibits excellent reproducibility (Figure 2c), suggesting the pronounced fatigue resistance of the system. Figure 2d shows the reflective color evolution of the BPLC q-plate during the shift of the electrically driven PBG under a polarized optical microscope (POM). Uniform and sharp reflection colors are observed, indicating that the superstructure is well maintained except for lattice stretching. The central dark spots correspond to the topological singularities. During the same process, the reflected light is encoded with the designed spiral phase. Accordingly, donut shaped vortex beams with corresponding colors are generated (Figure 2e).

2.3. Angle-Dependent Circular Polarization Selectivity and PBG Shift

The BPLC 3D photonic crystals exhibit angle-dependent light-modulation performance. We continuously change the angle α between a polarizer and the fast axis of a quarter wave plate

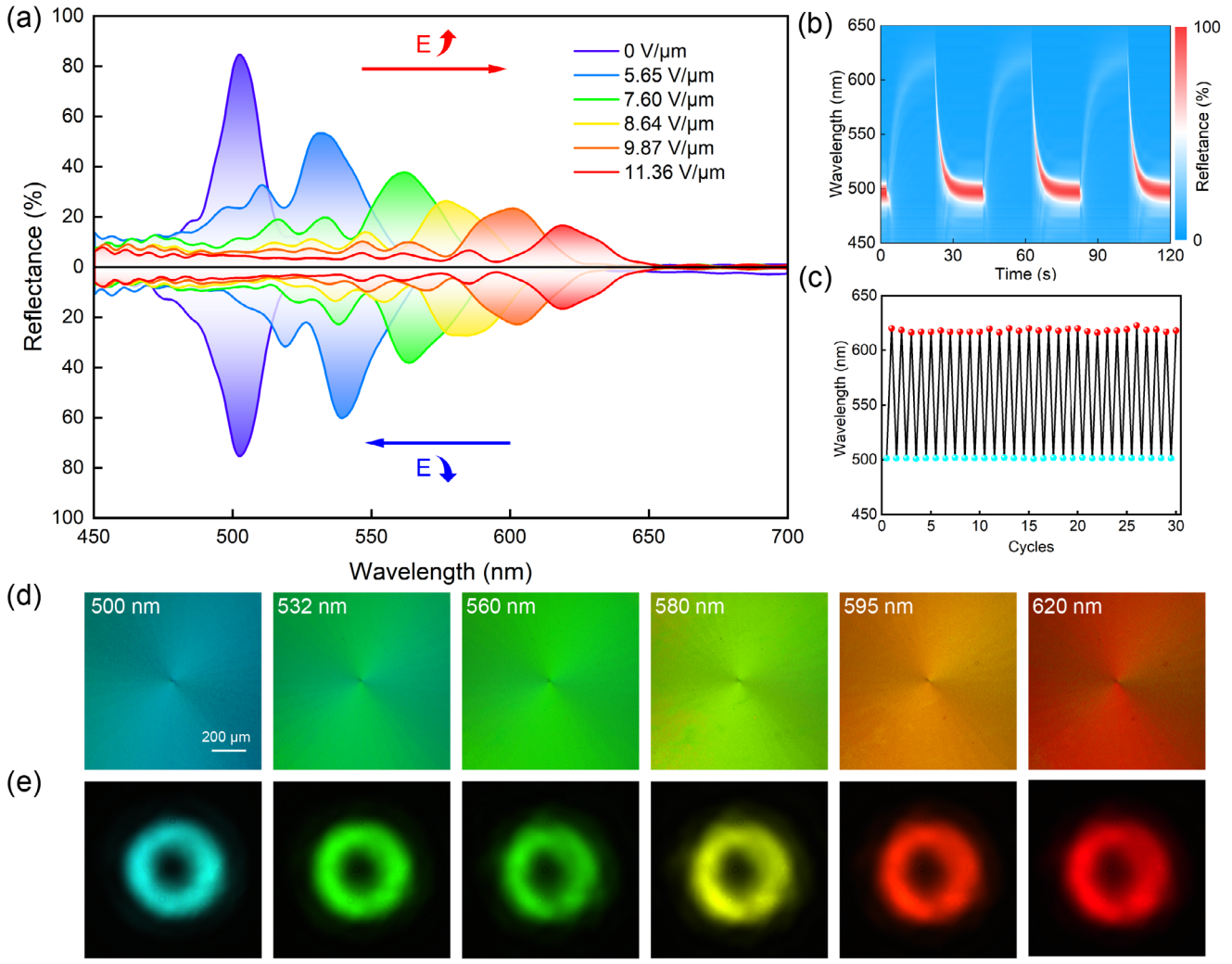

Figure 2. Electrically tuning PBG of the BPLC *q*-plate, which is made by sample M1: a) The reversible color shift induced by electrostriction of the BPLC for LCP incidence. b) Response time of the PBG shift. c) Fatigue resistance of the PBG shift. d) POM micrographs of the BPLC *q*-plate with λ_c = 500, 532, 560, 580, 595 and 620 nm. e) Correspondingly generated optical vortices for normal incidence.

to characterize the polarization selectivity of the BPLC *q*-plate. **Figure** 3a reveals the dependency of the reflectance on α for different incident angles of θ = 0°, 15°, 30° and 45°, respectively. As the utilized BPLC is left-handed, we can see only left-handed circularly polarized (LCP, α = 45° and 225°) light is selectively reflected, while the reflectance for right-handed circular polarization (RCP, α = 135° and 315°) is highly suppressed. The measured results match well with the theoretical simulations (Note S2, Supporting Information):

$$\eta = \cos^2\left(\frac{\pi}{4} - \alpha\right) \tag{3}$$

η *is* the efficiency of reflective output light E_{out}. Owing to the perfect circular polarization selectivity, the designed geometric phase equal to $2{\cdot}\beta(x, y)$ is encoded to the reflected light faithfully in a wide-angle range. Figure 3b shows the phase modulation related to circular polarization of the BPLC *q*-plate with θ = 45°. For LCP incidence, all light is reflected and transformed into an optical vortex with a topological charge of +1. For RCP incidence, the light is completely transmitted and a Gaussian beam is maintained. For linearly polarized (LP) incident light, the components of orthogonal circular polarization are split completely. The LCP is reflected and encoded with a spiral phase, while the RCP transmits directly as a Gaussian beam.

We further investigate the dependency of λ_c on θ. The blue curve in Figure 3c reveals the simulated dependency of λ_c on θ according to Bragg's equation [Equation (2)]. The dots record the experimental results. The deviation between them is due to refraction at the air/glass interface. The red curve calibrates the refraction and thus matches well with the experimental results (Note S3, Supporting Information). We systematically recorded the reflection spectra of the BPLC *q*-plate at various θ and E (Figure S6, Supporting Information) and drew a diagram of λ_c on θ and E. As shown in Figure 3d, θ and E influence λ_c oppositely, thus suggesting a compensation method. For a given wavelength, the compensating DC electric field can be directly searched from the diagram. We take 532-nm green light as an example, the DC

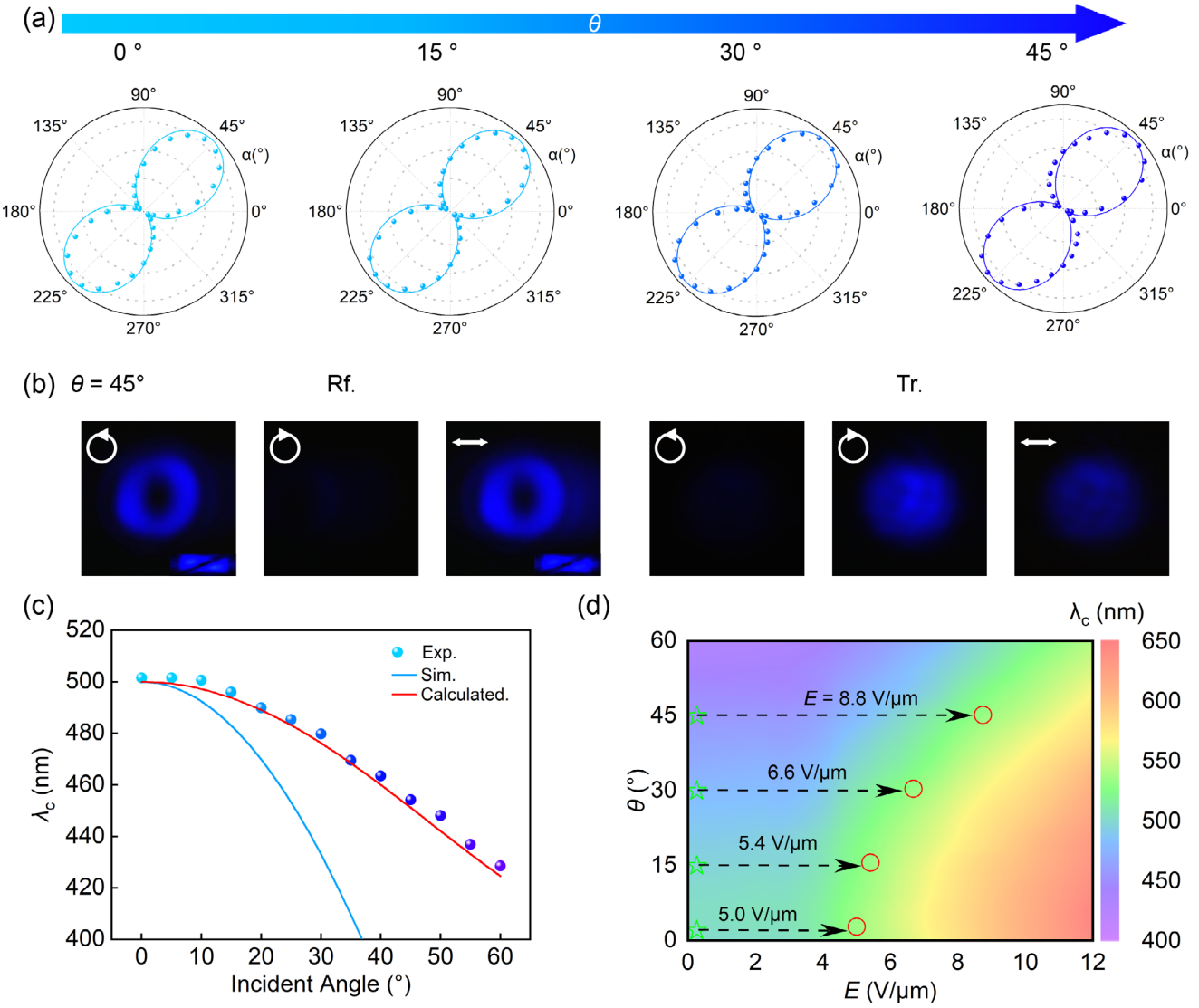

Figure 3. Angle-dependent performance of the BPLC *q*-plate: a) Circular polarization selectivity at incident angles of 0°, 15°, 30°= and 45°. b) Transmissive and reflective beams for different incident polarizations (LCP, RCP and LP) and $\theta = 45°$. The wavelength of the incident light is 460 nm c). Simulated and measured values of λ_c for different θ. d) Diagram showing the dependence of λ_c on θ and E.

electric fields E of 5.0, 5.4, 6.6 and 8.8 V μm^{-1} are required for compensation at $\theta = 0°$, 15°, 30° and 45°, respectively.

2.4. Monochromatic Large-Angle Optical Edge Imaging

Circular polarization selective phase encoding enables bifunctional imaging of the BPLC *q*-plate. As presented in **Figure** 4a, a transflective 4*f* imaging system with a rotatable holder (for *q*-plate) and reflection imaging part is constructed for characterization. Different monochromic lasers are separately output by a supercontinuum laser and pass through a polarizer and a broadband quarter waveplate to alternate orthogonal circular polarizations. A transmissive mask including a tulip and a cat serves as the amplitude-type object. The BPLC *q*-plate is set on the Fourier plane between Lens 1 and Lens 2/3, and the incidence angle is adjusted via rotating the holder. Two charge coupled devices (CCDs) are utilized to capture the bifunctional imaging: one is placed at the rear focal plane of Lens 2 to record the optical edge image, and the other is placed at the rear focal point of Lens 3 to record the bright-field image. Corresponding circular polarizers (CPs) are placed in front of each CCD to reduce the mirror reflection and thus improve the imaging quality. Figure 4b reveals the optical edge images recorded in the reflective path. We can see that both vertical and horizontal edges are clearly extracted. Figure 4c shows corresponding bright-field images recorded in the transmission path. The 1951 United States Air Force (USAF) resolution test chart is used to check the resolution for optical edge imaging. The edges of element 3 in group 3 can be distinguished successfully, whose resolution is 0.099 mm per line pair (Figure S7, Supporting Information). In addition to the amplitude-type object, the optical edges of phase-type objects such as etched glass

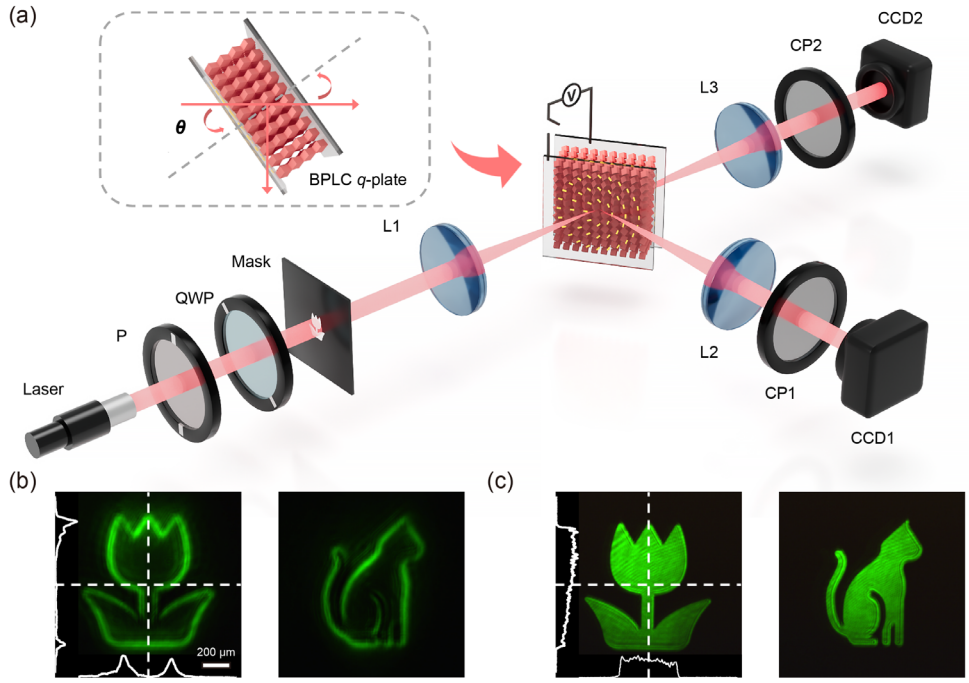

Figure 4. a) Optical setup for simultaneous reflective optical edge imaging and transmissive bright-field imaging. P is a polarizer, QWP is a quarter waveplate, L is the lens, and CP are circular polarizers, respectively. b) Optical edge images of a "tulip" and a "cat". c) Corresponding bright-field images. The focal length of all lenses is 150 mm, the aperture of masks is 1 mm × 1 mm and the diameter of the laser beam is 0.8 mm.

sides can also be detected as well (Figure S8, Supporting Information).

We investigate angle-dependent optical edge detection under oblique incidence conditions via rotating the BPLC *q*-plate. Two BPLCs (M1 and M2) with different chiral agent contents are adopted as examples. **Figure 5** shows the optical edge images recorded at $\theta = 0°$, 15°, 30°, and 45°. As mentioned previously, the same geometric phase is encoded to the reflected light omnidirectionally due to the 3D chiral photonic crystal feature of the photopatterned BPLC. Since the same spiral phase is encoded to the reflected light, the obtained edge information is consistent with the object. For comparison, the optical edge images captured with a traditional nematic *q*-plate suffer from severe distortions and sharpness decreases (Figure S9, Supporting Information). For nematic LC *q*-plates, distortions are inevitably induced in optical edge detection due to the incomplete geometric phase modulation for obliquely incident light, as the device is optimized only for the normal incidence. BPLC successfully overcomes this problem thanks to its omnidirectionally complete geometric phase encoding property. Notably, the central wavelength of the PBG changes according to Bragg's equation. Along with the increase of the incident angle, the color shifts from cyan to blue for M1 and from red to green for M2, whose combination covers the whole visible range. A fixed wavelength is commonly adopted in active optical edge imaging. To compensate for the angle-dependent color shift, the DC electric field exhibited in Figure 3d is applied to generate proper lattice extension for different oblique incidences. After compensation, the color variations are successfully eliminated for both M1 and M2. As revealed in the right part of Figure 5, the color (green and red) and wavelength (532 and 633 nm) of M1 and M2 are both fixed during ± 45° wide-angle optical edge imaging.

The proposed optical edge detection method shows superiorities in three aspects compared with previous ones: firstly, the BPLC *q*-plate omnidirectionally encodes the same spiral phase for optical differentiation to all reflected light, thus avoiding oblique incidence induced edge distortions and image contrast reduction; secondly, the electrostriction induced BPLC lattice extension precisely compensates the angle-dependent wavelength shift for oblique incidences; thirdly, thanks to the inherent circular polarization dependent phase modulation, monochromatic wide-angle optical edge imaging and bright field imaging are accomplished simultaneously. The method can be further optimized in several different directions: first of all, photosensitive chiral molecular switches doped BPLC or negative dielectric anisotropic LCs can be adopted to eliminate the reflectance loss caused by the LC tilting induced birefringence reduction.[38] For pure optical edge detection, a dual-BPLC-layer strategy with opposite chirality can be introduced to utilize both orthogonal incident polarization.[39] Subsequently, through wash-out and refilling ferroelectric LCs into the BPLC polymer template,[40] the response time can be significantly improved and real-time imaging can be expected. Finally, by adjusting the composition, especially the chiral dopant concentration of BPLCs, combined with DC electric field variation, the wavelength can be selected and fixed over a broad range. With the help of electrically adjustable reflection bands, 905 nm (the dominant wavelength adopted in LiDAR) feasible optical edge detectors can be realized. Applications in the telecom band and Terahertz band are still on the way.[41]

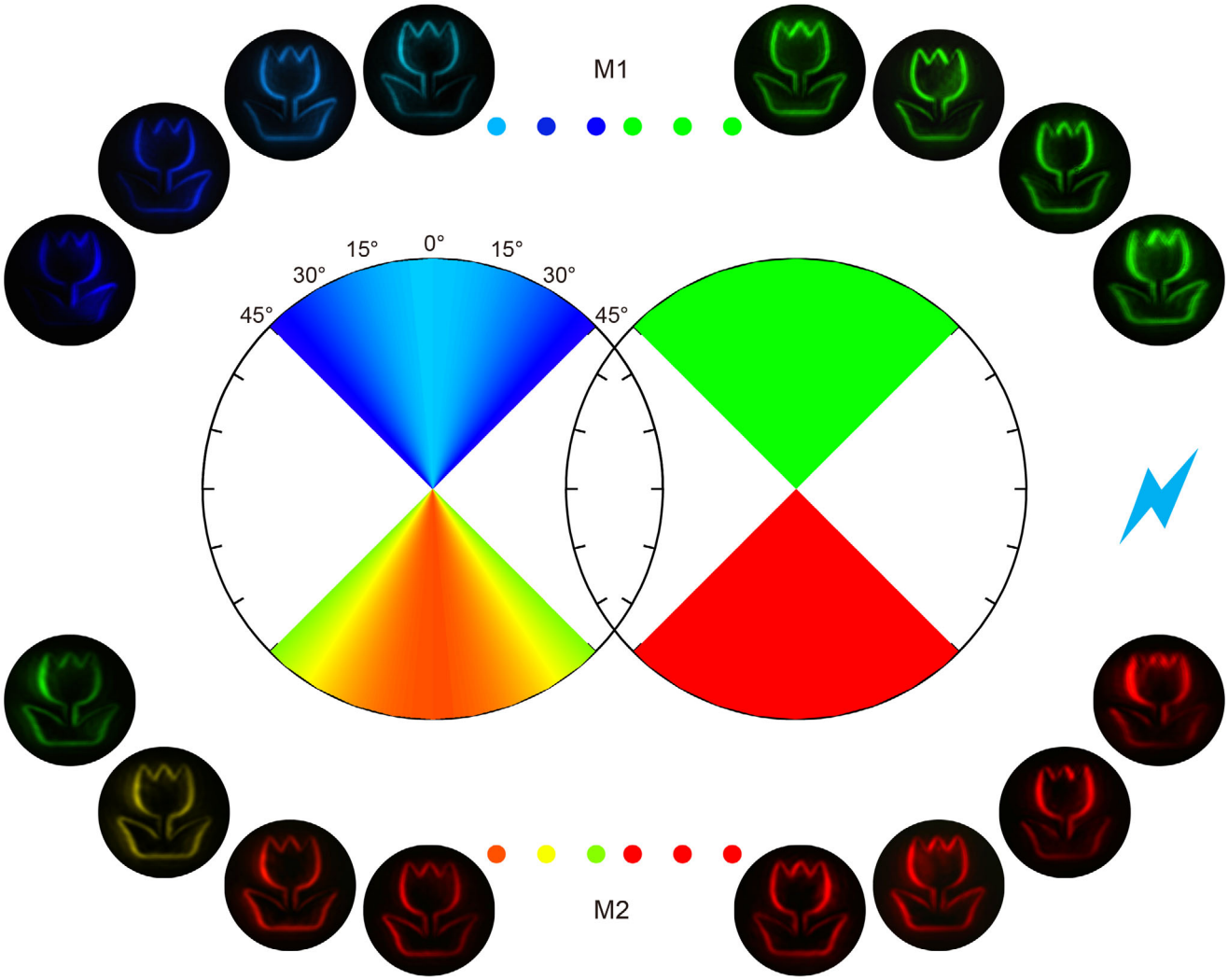

Figure 5. The two polar coordinates reveal the dependency of wavelength selectivity on incident angles. The left coordinate presents the angle dependent color shifts of optical edge imaging for M1 and M2 at $\theta = 0°$, 15°, 30° and 45°, respectively; and the right coordinate exhibits corresponding electrically compensated monochromatic wide-angle optical edge imaging. The colorful dots represent the omitting mirror-symmetric images when the incidence angle is $-\theta$ and θ for angle dependent color shifted and compensated optical edge imaging, respectively.

3. Conclusion

We propose and demonstrate a BPLC *q*-plate based bifunctional imaging system. It can perform monochromatic wide-angle optical edge detection in reflection mode while accomplishing bright-field imaging in transmission mode at the same time. The functions are realized due to the unique 3D photonic crystal configuration and electricity responsiveness of the photopatterned BPLCs. The circular polarization dependent phase modulation, omnidirectional phase encoding, and electrostriction induced lattice extension are responsible for the bifunction, wide-angle optical edge detection, and angle-dependent wavelength-shift compensation, respectively. This work reveals the great potential of soft materials in advanced photonics. This approach supplies a practical solution for active optical edge detection and may be further extended to wide applications that require the manipulation of monochromic waves at a wide angle.

4. Experimental Section

Materials: BPLCs were mixtures of host nematic LC HTW 114200-050 ($\Delta\epsilon$ = 10.9 at 1 kHz, 20 °C; Δn = 0.222 and n_e = 1.729 at 589 nm, 20 °C; HCCH, China), chiral dopant S811 (helical twisted power, HTP = 8.3 μm^{-1} at 30 °C), reactive mesogen RM257 (NCLCP, China), nonmesogen EHA (Sigma–Aldrich, USA), and photoinitiator Omnirad 651 (BASF, Germany), the corresponding chemical structure of the molecules in BPLC premix as shown in Table S1 (Supporting Information). BPLC sample M1 was mixed in a weight ratio of HTW114200-050/S811/RM257/EHA/Omnirad 651 = 55.5/36/4.0/4.0/0.5, and BPLC sample M2 was HTW114200-050/S811/RM257/EHA/Omnirad 651 = 59.5/32/4.0/4.0/0.5. After stirring evenly, the BPLC mixtures were capillarity filled into cells at 10 °C above the clearing points. Then, the sample was cooled at a rate of −0.3 °C min^{-1} using a hot stage (Linkam, UK) until the emergence of BP I. An AC electric field (32.5 V μm^{-1}, 1 kHz) was applied for 1 min at 0.5 °C below the BP II-BP I phase transition point and monodomain BP I was obtained. A 365 nm LED (Thorlabs, USA) was used to illuminate the samples for 60 min at 40 $\mu W\ cm^{-2}$ for UV polymerization.

Photopatterning and Cell Fabrication: Indium-tin-oxide coated glass was ultrasonically cleaned, UV-ozone treated, and spin-coated with photoalignment agent SD 1 (NCLCP, China) at a concentration of 0.3 wt.% dissolved in dimethyl formamide (DMF, Sigma–Aldrich, USA). Then, the samples were baked at 100 °C for 10 min. Two glass substrates were separated by epoxy resin glue doped with 7.7-µm spacer. The photopatterning was performed with a digital-micromirror-device based polarization microlithography system (NCLCP, China).[42]

Characterizations: The reflection spectra were recorded using a spectrometer (PG2000-pro, Ideaoptics, China) with structure helicity matched circularly polarized incidence. All the micrographs were taken under a polarizing microscope (Nikon 50i, Japan) in reflection mode. The monochromatic and white beams were output by a supercontinuum laser (SuperK EVO, NKT Photonics, Denmark) and multi-channel acousto-optic tunable filters (SuperK SELECT, NKT Photonics, Denmark). The polarizer combined with a quarter wave plate (JCOPTIX, China) to sort different circularly polarized light. The optical edge detection images were captured by a CCD. The 1 kHz AC square-wave electrical signal and DC electrical signal were generated by a function generator (33522 B, Agilent, USA) and amplified by a voltage amplifier (2340, TEGAM, USA).

Supporting Information

Supporting Information is available from the Wiley Online Library or from the author.

Acknowledgements

Z.X. and Q.C. contributed equally to this work. The authors gratefully acknowledge the support of the National Key Research and Development Program of China (2022YFA1203700), the National Natural Science Foundation of China (NSFC) (T2488302, 62035008 and 62405127), the Natural Science Foundation of Jiangsu Province (BK20233001), the Fundamental Research Funds for the Central Universities (021314380244), and the Postdoctoral Fellowship Program of CPSF under Grant Number (GZC20240640). The authors gratefully appreciate JCOPTIX for providing the optical test equipment. The authors appreciate Zhenghao Guo and Guangyao Wang for their constructive discussions.

Conflict of Interest

The authors declare no conflict of interest.

Data Availability Statement

The data that support the findings of this study are available from the corresponding author upon reasonable request.

Keywords

blue phase liquid crystal, geometric phase, liquid crystal photonics, optical edge detection

Received: January 10, 2025
Revised: May 1, 2025
Published online: May 15, 2025

[1] F. L. Bao, X. J. Wang, S. H. Sureshbabu, G. Sreekumar, L. P. Yang, V. Aggarwal, V. N. Boddeti, Z. Jacob, *Nature* **2023**, *619*, 743.
[2] a) Y. X. Ban, M. Z. Liu, P. Wu, B. Yang, S. Liu, L. R. Yin, W. F. Zheng, *Electronics* **2022**, *11*, 2012; b) G. Vicidomini, P. Bianchini, A. Diaspro, *Nat. Methods* **2018**, *15*, 173.
[3] C. Rogers, A. Y. Piggott, D. J. Thomson, R. F. Wiser, I. E. Opris, S. A. Fortune, A. J. Compston, A. Gondarenko, F. F. Meng, X. Chen, G. T. Reed, R. Nicolaescu, *Nature* **2021**, *590*, 256.
[4] a) H. J. Caulfield, S. Dolev, *Nat. Photonics* **2010**, *4*, 261; b) D. R. Solli, B. Jalali, *Nat. Photonics* **2015**, *9*, 704.
[5] S. S. He, J. X. Zhou, S. Z. Chen, W. X. Shu, H. L. Luo, S. C. Wen, *APL Photonics* **2020**, *5*, 036105.
[6] D. Y. Xu, S. S. He, J. X. Zhou, S. Z. Chen, S. C. Wen, H. L. Luo, *Appl. Phys. Lett.* **2020**, *116*, 211103.
[7] a) H. W. Yang, W. C. Xie, H. F. Chen, M. Y. Xie, J. Y. Tang, H. D. Zheng, Y. C. Zhong, J. H. Yu, Z. Chen, W. G. Zhu, *Optica* **2024**, *11*, 1008; b) B. W. Song, S. C. Wen, W. X. Shu, *ACS Photonics* **2022**, *9*, 3987.
[8] T. F. Zhu, Y. H. Zhou, Y. J. Lou, H. Ye, M. Qiu, Z. C. Ruan, S. H. Fan, *Nat. Commun.* **2017**, *8*, 15391.
[9] a) Y. Z. Zhang, P. C. Lin, P. C. Huo, M. Z. Liu, Y. Z. Ren, S. Zhang, Q. W. Zhou, Y. L. Wang, Y. Q. Lu, T. Xu, *Nano Lett.* **2023**, *23*, 2991; b) F. Mei, G. Y. Qu, X. B. Sha, J. Han, M. X. Yu, H. Li, Q. M. Chen, Z. H. Ji, J. C. Ni, C. W. Qiu, Q. H. Song, Y. Kivshar, S. M. Xiao, *Nat. Commun.* **2023**, *14*, 6410; c) Y. Kim, G. Y. Lee, J. Sung, J. Jang, B. Lee, *Adv. Funct. Mater.* **2021**, *32*, 2106050.
[10] Y. Zhou, H. Zheng, I. I. Kravchenko, J. Valentine, *Nat. Photonics* **2020**, *14*, 316.
[11] J. X. Zhou, H. L. Qian, C. F. Chen, J. X. Zhao, G. R. Li, Q. Y. Wu, H. L. Luo, S. C. Wen, Z. W. Liu, *P Natl. Acad. Sci. USA* **2019**, *116*, 11137.
[12] a) Z. Y. Wang, Z. Zhou, H. Zhang, Y. Wei, H. G. Yu, W. Hu, W. Chen, H. T. Dai, L. L. Ma, C. W. Qiu, Y. Q. Lu, *Elight* **2024**, *4*, 5; b) G. Y. Wang, H. Cao, Z. H. Guo, C. T. Xu, Q. M. Chen, W. Hu, *Adv. Photonics Nexus* **2025**, *4*, 025001.
[13] S. J. Liu, L. Zhu, Y. H. Zhang, W. Chen, D. Zhu, P. Chen, Y. Q. Lu, *Adv. Mater.* **2023**, *35*, 2301714.
[14] Q. G. Wang, S. J. Ge, H. G. Yu, W. Hu, *Laser Photonics Rev.* **2024**, *18*, 2400869.
[15] S. Q. Liu, F. Fan, S. Z. Chen, S. C. Wen, H. L. Luo, *Laser Photonics Rev.* **2023**, *17*, 2300044.
[16] X. Liang, D. Zhu, Q. Dai, Y. X. Xie, Z. Zhou, C. Peng, Z. L. Li, P. Chen, Y. Q. Lu, S. H. Yu, G. X. Zheng, *Laser Photonics Rev.* **2024**, *18*, 2400032.
[17] W. Chen, D. Zhu, S. J. Liu, Y. H. Zhang, L. Zhu, C. Y. Li, S. J. Ge, P. Chen, W. L. Zhang, X. C. Yuan, Y. Q. Lu, *Natl. Sci. Rev.* **2024**, *11*, 247.
[18] Q. M. Chen, H. C. Wang, G. Y. Wang, C. T. Xu, Q. G. Tan, W. Duan, Y. Q. Lu, W. Hu, *Appl. Phys. Lett.* **2023**, *123*, 251101.
[19] D. Zhu, Y. H. Zhang, S. J. Liu, W. Chen, L. Zhu, S. J. Ge, P. Chen, W. Duan, Y. Q. Lu, *Nano Lett.* **2023**, *24*, 140.
[20] a) J. Liu, W. Z. Liu, B. Guan, B. Wang, L. Shi, F. Jin, Z. G. Zheng, J. X. Wang, T. Ikeda, L. Jiang, *Nat. Commun.* **2021**, *12*, 3477; b) Y. J. Chen, C. L. Zheng, W. J. Yang, J. Li, F. Jin, L. Shi, J. X. Wang, L. Jiang, *Adv. Mater.* **2024**, *36*, 2308439; c) J. A. Martínez-González, X. Li, M. Sadati, Y. Zhou, R. Zhang, P. F. Nealey, J. J. de Pablo, *Nat. Commun.* **2017**, *8*, 15854; d) K. Bagchi, T. Emersic, J. A. Martínez-González, J. J. de Pablo, P. F. Nealey, *Sci. Adv.* **2023**, *9*, adh9393; e) D. C. Wright, N. D. Mermin, *Rev. Mod. Phys.* **1989**, *61*, 385.
[21] Y. Q. Guo, M. Z. Fu, Y. X. Ren, Y. F. Wang, Q. H. Mu, H. M. Ma, J. L. Zhu, Y. B. Sun, *Liq. Cryst.* **2017**, *44*, 2321.
[22] S. Y. Cho, M. Takahashi, J. Fukuda, H. Yoshida, M. Ozaki, *Commun. Mater.* **2021**, *2*, 39.
[23] Q. M. Chen, X. Y. Wang, C. T. Xu, H. C. Chu, H. G. Yu, C. Ouyang, Y. Lai, Z. G. Zheng, X. Liang, Y. Q. Lu, W. Hu, *Laser Photonics Rev.* **2024**, *18*, 2301283.
[24] W. Hu, J. Sun, Q. Wang, L. Y. Zhang, X. T. Yuan, F. W. Chen, K. X. Li, Z. C. Miao, D. K. Yang, H. F. Yu, H. Yang, *Adv. Funct. Mater.* **2020**, *30*, 2004610.

[25] S. A. Jiang, C. H. Wu, T. S. Mo, S. Y. Huang, J. D. Lin, C. R. Lee, *Crystals* **2020**, *10*, 906.
[26] X. J. Xu, H. Gao, S. Q. Ren, C. L. Zheng, K. Y. Du, X. Zhou, Z. C. Ye, J. L. Zhu, J. X. Wang, L. Jiang, *Small* **2024**, *20*, 2310048.
[27] a) R. Manda, S. Pagidi, Y. Heo, Y. J. Lim, M. Kim, S. H. Lee, *NPG Asia Mater.* **2020**, *12*, 42; b) T. H. Lin, D. Y. Guo, C. W. Chen, T. M. Feng, W. X. Zeng, P. C. Chen, L. Y. Wu, W. M. Guo, L. M. Chang, H. C. Jau, C. T. Wang, T. J. Bunning, I. C. Khoo, *Nat. Commun.* **2024**, *15*, 7038; c) S. Y. Lu, L. C. Chien, *Opt. Lett.* **2010**, *35*, 562.
[28] Y. Hisakado, H. Kikuchi, T. Nagamura, T. Kajiyama, *Adv. Mater.* **2005**, *17*, 96.
[29] G. P. Alexander, D. Marenduzzo, *EPL* **2008**, *81*, 66004.
[30] D. Y. Guo, C. W. Chen, C. C. Li, H. C. Jau, K. H. Lin, T. M. Feng, C. T. Wang, T. J. Bunning, I. C. Khoo, T. H. Lin, *Nat. Mater.* **2020**, *19*, 94.
[31] Q. M. Chen, C. Ouyang, Z. Y. Xie, C. T. Xu, Z. X. Wu, J. Y. Min, Y. J. Liu, D. Luo, W. Hu, *Laser Photonics Rev.* **2025**, *19*, 2401635.
[32] S. J. Ge, W. Ji, G. X. Cui, B. Y. Wei, W. Hu, Y. Q. Lu, *Opt. Mater. Express* **2014**, *4*, 2535.
[33] a) H. Yoshida, J. Kobashi, *Liq. Cryst.* **2016**, *43*, 1909; b) J. Kobashi, H. Yoshida, M. Ozaki, *Nat. Photonics* **2016**, *10*, 389.
[34] C. W. Chen, C. C. Li, H. C. Jau, L. C. Yu, C. L. Hong, D. Y. Guo, C. T. Wang, T. H. Lin, *ACS Photonics* **2015**, *2*, 1524.
[35] a) M. Wang, C. Zou, C. Y. Li, J. Sun, L. Wang, W. Hu, C. H. Zhang, L. Y. Zhang, W. L. He, H. Yang, *Adv. Opt. Mater.* **2018**, *6*, 1800409; b) M. Wang, C. Zou, J. Sun, L. Y. Zhang, L. Wang, J. M. Xiao, F. S. Li, P. Song, H. Yang, *Adv. Funct. Mater.* **2017**, *27*, 1702261.
[36] a) H. Kikuchi, M. Yokota, Y. Hisakado, H. Yang, T. Kajiyama, *Nat. Mater.* **2002**, *1*, 64; b) J. Yan, H. C. Cheng, S. Gauza, Y. Li, M. Z. Jiao, L. H. Rao, S. T. Wu, *Appl. Phys. Lett.* **2010**, *96*, 071105.
[37] C. W. Chen, C. T. Hou, C. C. Li, H. C. Jau, C. T. Wang, C. L. Hong, D. Y. Guo, C. Y. Wang, S. P. Chiang, T. J. Bunning, I. C. Khoo, T. H. Lin, *Nat. Commun.* **2017**, *8*, 727.
[38] C. T. Xu, D. W. Zhang, R. Yuan, Q. M. Chen, X. Liang, W. Hu, *Laser Photonics Rev.* **2023**, *17*, 2201013.
[39] a) W. J. Yang, C. L. Zheng, L. Sun, Z. Y. Bie, Y. C. Yue, X. H. Li, W. T. Sun, T. Ikeda, J. X. Wang, L. Jiang, *Adv. Mater.* **2025**, *37*, 2411988; b) X. W. Xu, Z. Liu, Y. J. Liu, X. H. Zhang, Z. G. Zheng, D. Luo, X. W. Sun, *Adv. Opt. Mater.* **2018**, *6*, 1700891.
[40] K. Nakajima, H. Kamifuji, M. Nakase, K. Nishi, H. Kikuchi, M. Ozaki, *Acs Appl Mater Inter* **2024**, *16*, 66552.
[41] Q. F. Liu, D. Luo, X. H. Zhang, S. X. Li, Z. Tian, *Liq. Cryst.* **2017**, *44*, 348.
[42] P. Chen, B. Y. Wei, W. Hu, Y. Q. Lu, *Adv. Mater.* **2019**, *32*, 1903665.

